Proposal for the formation of ultracold deeply bound RbSr dipolar molecules by all-optical methods

Adrien Devolder,[1,*] Eliane Luc-Koenig,[1] Osman Atabek,[2] Michèle Desouter-Lecomte,[3] and Olivier Dulieu[1]

[1]*Laboratoire Aimé Cotton, CNRS, Université Paris-Saclay, Univ. Paris-Sud, ENS Paris-Saclay, Bât. 505, 91405 Orsay Cedex, France*

[2]*Institut des Sciences Moléculaires d'Orsay (ISMO, UMR8214) CNRS, Université Paris-Saclay, Univ. Paris-Sud, Bât. 520, 91405, Orsay, France*

[3]*Laboratoire de Chimie Physique (LCP, UMR 8000) CNRS, Université Paris-Saclay, Univ. Paris-Sud, Bât. 349, 91405, Orsay, France*

(Received 27 June 2018; published 9 November 2018)

Ultracold paramagnetic and polar diatomic molecules are among the promising systems for quantum simulation of lattice-spin models. Unfortunately, their experimental observation is still challenging. Based on our recent *ab initio* calculations, we analyze the feasibility of all-optical schemes for the formation of ultracold ^{87}Rb^{84}Sr bosonic molecules. A first possibility is photoassociation followed by spontaneous emission. The photoassociation rate coefficients toward electronic states converging to the $^{87}\mathrm{Rb}(5s\,^2S_{1/2}) + {}^{84}\mathrm{Sr}(5s5p\,^3P_{0,1,2})$ asymptotes are particularly small for vibrational levels close to the asymptote. The creation of molecules would be more interesting by using deeply bound levels which preferentially relax to the $v'' = 0$ level of the ground state. On the other hand, the photoassociation rate coefficients toward electronic states correlated to the $\mathrm{Rb}(5p\,^2P_{1/2,3/2}) + \mathrm{Sr}(5s^2\,^1S_0)$ are significant for levels close to the asymptote. The spontaneous emission thus creates weakly bound molecules in a single vibrational level. A second option relies on stimulated Raman adiabatic passage implemented in a tight optical trap. It efficiently creates weakly bound ground-state molecules in a well-defined level, thus providing a promising alternative to magnetic Feshbach resonances for further population transfer toward the absolute ground state of the RbSr molecule.

DOI: 10.1103/PhysRevA.98.053411

I. INTRODUCTION

Ultracold diatomic molecules, namely with translational motion cooled down to temperatures well below one millikelvin, and internal degrees of freedom reduced to a single quantum level [1], are nowadays well recognized as promising systems for quantum simulation, quantum computation, ultracold chemistry, and precision measurements. This is particularly true for those species which possess additional internal properties like a permanent electric dipole moment (PEDM) in their own frame and/or a magnetic dipole moment, as they can be manipulated by external electric and magnetic fields [2–6].

The translationally ultracold molecular species produced were homonuclear, namely Cs_2 [7] and Rb_2 molecules [8]. The formation process relied on photoassociation (PA) of ultracold atomic pairs followed by radiative emission (RE) down to the electronic ground state [9]. Shortly after, several groups were able to create heteronuclear diatomic species with the same approach [10]. A breakthrough came with the direct observation of ultracold molecule formation (UMF) in the lowest rovibrational level ($v'' = 0$, $J'' = 0$) of their ground state [11], with some ability of control of their internal state [12–14]. The fully controlled creation of ultracold dipolar molecules was demonstrated at about the same time on the KRb polar species [15–17], but using the alternative approach of magnetoassociation of an atom pair into a weakly bound molecule, followed by a stimulated Raman adiabatic passage (STIRAP) to transfer population into the lowest-energy level of the KRb electronic ground state.

Ground-state species exhibiting an additional magnetic moment are for instance diatomic molecules composed of an alkali-metal atom and an alkaline-earth atom (or an ytterbium atom), in which the magnetic dipole moment comes from the existence of an unpaired electron. Surprisingly, the spectroscopy of such diatomic molecules is still poorly known. The recent interest for such ultracold species triggered several investigations at relatively low resolution [18–23]. However, these species are still challenging to create in the ultracold domain. After an initial prediction [24], magnetic Feshbach resonances have been observed for ^{87}Rb^{88}Sr and ^{87}Rb^{87}Sr molecules [25], but they are not yet used for the formation of weakly bound ground-state molecules.

All-optical methods are attractive to create ultracold molecules as they do not rely on peculiarities of their molecular structure like the presence of Feshbach resonances in the ground state at moderate magnetic fields. Here we model the PA+RE sequence for the ^{87}Rb^{84}Sr bosonic species. As expected we find that it is not selective enough to populate a single quantum level in the molecular ground state. Therefore, we consider the motional levels of a tight optical trap [26] to implement a STIRAP transfer, as previously demonstrated with Sr_2 molecules [27,28]. Our calculations are based on the RbSr electronic structure data previously obtained in our group [29,30], which are recalled in Sec. II. We compute in Sec. III PA and UMF rate coefficients, when the PA laser is tuned to the red of either the $(5\,^2S_{1/2} \rightarrow 5\,^2P_{1/2,3/2})$ resonant transitions in ^{87}Rb or of the $(5\,^1S_0 \rightarrow 5\,^3P_{0,1,2})$ intercombination transitions in ^{84}Sr. The transition $^1S_0 \rightarrow {}^3P_1$ is indeed employed for the cooling of Sr atoms in ongoing experiments

*adrien.devolder@u-psud.fr

on quantum degenerate mixtures of strontium and rubidium atoms [31]. Relying on the obtained knowledge about transition dipole moments, we propose promising candidate levels to implement the STIRAP process in a tight optical trap to create weakly bound ultracold $^{87}Rb^{84}Sr$ ground-state molecules (Sec. IV), and to transfer them in the lowest vibrational level using a second STIRAP sequence (Sec. V). For the purpose of convenience in the calculations, atomic units of distance (1 a.u. $= a_0 = 0.052917721067$ nm), energy (1 a.u. $=$ 1 hartree $= 219474.6313702\,\mathrm{cm}^{-1}$), and electric dipole moment (1 a.u. $= 2.54175$ D) will be used throughout the0 paper, except otherwise stated.

II. ELECTRONIC STRUCTURE OF THE RbSr MOLECULE

In this work, we are interested in the states correlated to the three lowest dissociation limits of RbSr (turning into six limits when spin-orbit interaction is included), listed with increasing energy: Rb $(5s\,^2S)$ + Sr $(5s^2\,^1S)$, Rb $(5p\,^2P)$ + Sr $(5s^2\,^1S)$, and

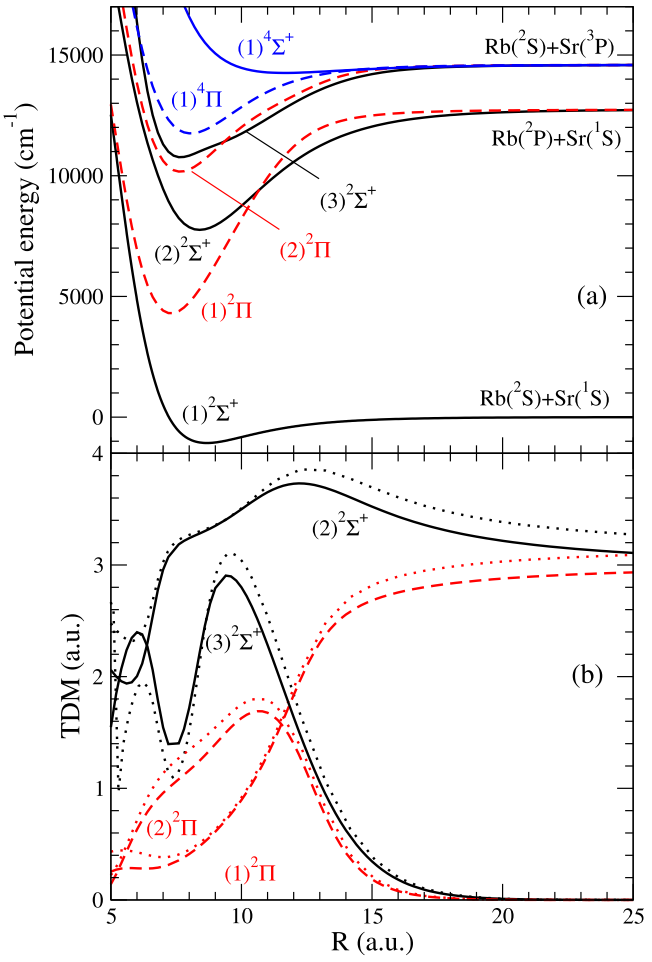

FIG. 1. (a) Potential-energy curves of the electronic states relevant for the present study. (b) Transition dipole moments between the $X^2\Sigma^+$ ground state and the (2,3) $^2\Sigma^+$ and (1,2) $^2\Pi$ states [30] (solid and dashed lines), compared to those of Ref. [32] (dotted lines). We note that our computed TDMs properly match the atomic TDMs at large distances, while those of Ref. [32] are overestimated by about 10% at this limit.

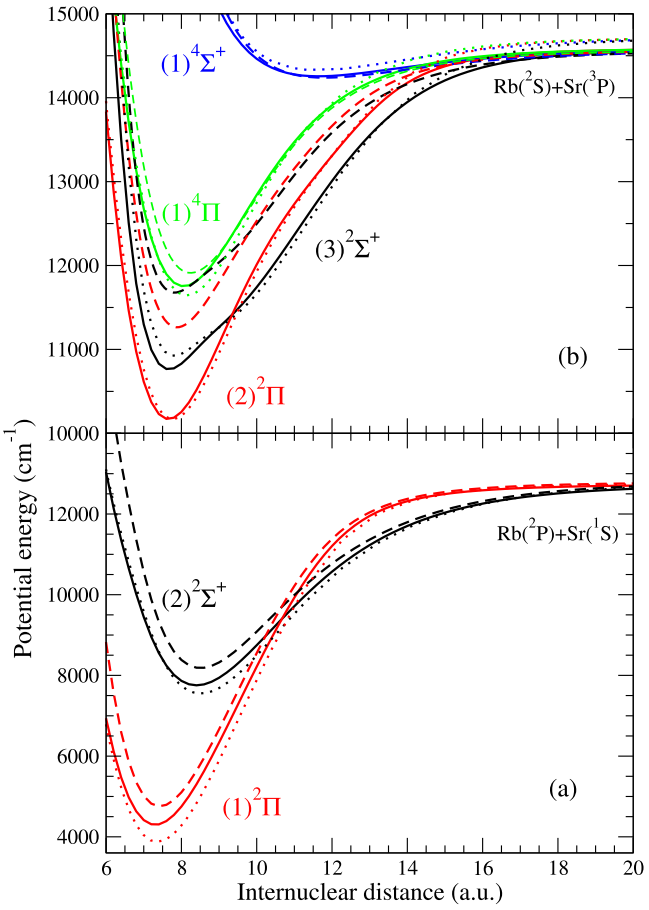

FIG. 2. Comparison of potential-energy curves of the lowest excited states of RbSr calculated with FCI(ECP+CPP) (solid lines), EOM-CC (dashed lines) [30], and MCSCF-MRCI (dotted lines) [32] methods.

Rb $(5s\,^2S)$ + Sr $(5s5p\,^3P)$. They give rise to three sets of electronic states [labeled in Hund's case (a) notation $(N)^{2S+1}\Lambda$], namely $(1)^2\Sigma^+$, or more commonly $X\,^2\Sigma^+$, $[(2)^2\Sigma^+, (1)^2\Pi]$, and $[(3)^2\Sigma^+, (1)^2\Pi, (1)^4\Sigma^+, (1)^4\Pi]$, respectively. The corresponding potential-energy curves (PECs) and transition dipole moments (TDMs) between the $X\,^2\Sigma^+$ ground state and several excited electronic states are displayed in Fig. 1. For the next sections, we have selected in Ref. [30] the full configuration-interaction (FCI) calculations performed on the three valence electrons moving in the field of relativistic large effective core potentials (ECPs), including core-polarization potentials (CPPs), and extrapolated to large distances.

Several features of the PECs are important to notice for the following. Except for the $(1)^4\Sigma^+$ state, the equilibrium distances of excited-state PECs are smaller than the one of the ground-state PEC. Second, two curve crossings are visible, between the $(2)^2\Sigma^+$ and $(1)^2\Pi$ PECs and between the $(3)^2\Sigma^+$ and $(2)^2\Pi$ PECs. Note that a third crossing occurs at short distances (around $6a_0$) in the repulsive branch of the $(3)^2\Sigma^+$ and $(1)^4\Pi$ PECs, at an energy somewhat higher than their dissociation limit. These features are also present in two other available calculations displayed in Fig. 2 from very different methods, namely the EOM-CCSD (equation-of-motion coupled-cluster method limited to singly and

TABLE I. Main spectroscopic constants of the $^{87}Rb^{84}Sr$ electronic states correlated to the three lowest dissociation limits. The shortened labels "FCI" and "CCSD" for Ref. [30] refer to the calculations with the FCI(ECP+CPP) method and the EOM-CCSD method, respectively (see text).

State	R_e (a_0)	D_e (cm^{-1})	ω_e (cm^{-1})	C_6 [33] (a.u.)	Dissociation limit	Ref.
$(X)^2\Sigma^+$	8.69	1073.3	38.98	3699	$Rb(5s\,^2S) + Sr(5s^2\,^1S)$	[30] (FCI)
	8.82	1040.5	38.09			[30] (CCSD)
	8.65	1283.5	42.1			[32]
	8.827	1017.58	36.017			[34]
$(2)^2\Sigma^+$	8.40	4982.9	58.37	23324	$Rb(5p\,^2P) + Sr(5s^2\,^1S)$	[30] (FCI)
	8.51	4609.6	60.20			[30] (CCSD)
	8.54	5144.3	58.9			[32]
$(1)^2\Pi$	7.31	8439.8	79.50	8436		[30] (FCI)
	7.42	8038.6	83.19			[30] (CCSD)
	7.39	8770.2	79.5			[32]
$(3)^2\Sigma^+$	7.67	3828.0	65.26	8929	$Rb(5s\,^2S) + Sr(5s5p\,^3P)$	[30] (FCI)
	7.81	2892.4	62.48			[30] (CCSD)
	7.84	3677.8	57.4			[32]
$(2)^2\Pi$	7.65	4421.2	67.60	5716		[30] (FCI)
	7.88	3303.5	63.37			[30] (CCSD)
	7.80	4450.3	65.8			[32]
$(1)^4\Sigma^+$	11.63	336.3	15.42	8929		[30] (FCI)
	11.81	329.2	15.03			[30] (CCSD)
	11.64	396.7	16.			[32]
$(1)^4\Pi$	8.06	2838.1	56.98	5716		[30] (FCI)
	8.24	2655.7	54.95			[30] (CCSD)
	8.16	3053.9	57.6			[32]

doubly excited configurations) method employed in Ref. [30], and the MCSCF-MRCI (multiconfigurational self-consistent field-multi-reference configuration interaction) method of Ref. [32]. Figure 2 reveals a good overall agreement among all the results, recalling however that the EOM-CCSD results for the excited electronic states are probably less accurate than the other results, as already discussed in Ref. [30]. We also note in Fig. 2(b) that the PECs from Ref. [32] converge to a dissociation energy larger by $107\,cm^{-1}$ than ours. This is related to the excitation energy of the $Sr(5s5p\,^3P)$ level, found $20\,cm^{-1}$ above ($87\,cm^{-1}$ below) the experimental one, in the MCSCF-MRCI calculations (in the FCI and EOM-CCSD calculations [29,30]). In order to illustrate in a complementary way the above results, we display in Table I the spectroscopic constants of these PECs, as well as the coefficient C_6 of the leading-order term of the long-range van der Waals interaction between Rb and Sr [33]. For the ground state, the results of Chen *et al.* [34] are also included. Deeply bound spectra at high temperature and low resolution with thermoluminescence and laser-induced fluorescence between the $(X)^2\Sigma^+$ and $(2)^2\Sigma^+$ states have been recorded in Ref. [23]. The simulated fluorescence spectra using PECs from FCI(ECP+CPP), EOM-CCSD, and MSCF-MRCI calculations well reproduce the experiments with a better precision for the MSCF-MRCI calculation. The spectra from the EOM-CCSD calculations exhibit an important spectral shift due to less accuracy for the excited-state potentials. The measured vibrational constant is $42 \pm 5\ cm^{-1}$. The comparison with the theoretical values again shows the same tendency for the precision: MSCF-MRCI > FCI(ECP+CPP) > EOM-CCSD.

It is well known that a model for a PA spectrum depends on two crucial inputs: the long-range behavior of the PECs of the relevant states and the scattering length of the ground state. Therefore, the $(X)^2\Sigma^+$ ground-state PEC has been smoothly matched at $15a_0$ to an asymptotic expansion expressed as $-C_6/R^6 - C_8/R^8 - C_{10}/R^{10}$, with $C_6 = 3699$ a.u., $C_8 = 4.609 \times 10^5$ a.u., and $C_{10} = 5.833 \times 10^7$ a.u. [33]. In contrast, the long-range expansion of the excited-state PECs has been restricted to the $-C_6/R^6$ term (Table I).

In the absence of a global PEC determined spectroscopically for the ground state, one cannot rely on the scattering length provided by the computed PEC. However, the binding energies of the two uppermost vibrational levels of the $^{87}Rb^{84}Sr$ molecule relative to the Rb ($5s\,^2S$, $F = 1$) + Sr ($5s^2\,^1S$) limit (where F denotes the total angular momentum of the Rb atom including for the nuclear spin) have been recently measured in Ref. [23] in a two-photon photoassociation experiment, yielding to $9.67 \times 10^{-4}\,cm^{-1}$ and $2.49\,cm^{-1}$. Therefore, we have slightly modified the position of the repulsive wall of the PEC in order to match these experimental energies. The calculations of ground-state eigenenergies were performed with the mapped Fourier grid Hamiltonian method (MFGH) [35–38], using a grid extending from $R_{min} = 5a_0$ to $R_{max} = 2000a_0$, containing up to 1551 points. We have checked the convergence of the calculations with the size of the grid. The adjustment was constrained to the condition that the spectroscopic data of Table I remain unchanged (i.e., the bottom of the PEC is unchanged). The best agreement was found when moving the inner turning point by $0.042a_0$ toward smaller distances. After this adjustment, the scattering length

has a value of 89.3 a.u., which is close to the experimental one (92.7 a.u.) [23].

Important features of TDMs can be pointed out that may have a strong influence on the optical response of RbSr molecules. First, the spin selection rule forbids transitions between doublet and quartet states. Second, the atomic transition Rb $(5s\,^2S) \rightarrow$ Rb $(5p\,^2P)$ is allowed while the atomic transition Sr $(5s^2\,^1S) \rightarrow$ Sr $(5s^2\,^3P)$ is spin forbidden. This atomic selection rule is visible in the long-range part of the TDMs in Fig. 1(b). Finally, at short range, the TDM of the $X\,^2\Sigma^+$ ground state with the $(2)^2\Sigma^+$ state is large (around 2 a.u.), while the one with the $(1)^2\Pi$ state is as low as 0.4 a.u.

The spin-orbit (SO) splitting being large for the lowest excited states of both atoms ($\Delta_{\rm fs}^{\rm Rb} = 237.1\,{\rm cm}^{-1}$ and $\Delta_{\rm fs}^{\rm Sr} = 581.1\,{\rm cm}^{-1}$), they must be taken into account to model the PA spectrum. We used the same approach as in Ref. [30]: first the two sets of PECs correlated to the Rb $(5p\,^2P)$ + Sr $(5s^2\,^1S)$ and Rb $(5s\,^2S)$ + Sr $(5s5p\,^3P)$ dissociation limits are considered independently, and the atomic SO operators $\hat{W}_{\rm so}^{\rm Rb} = A^{\rm Rb}\vec{\ell}^{\rm Rb}\cdot\vec{s}^{\rm Rb}$ and $\hat{W}_{\rm so}^{\rm Sr} = A^{\rm Sr}(\vec{\ell}_1^{\rm Sr}\cdot\vec{s}_1^{\rm Sr} + \vec{\ell}_2^{\rm Sr}\cdot\vec{s}_2^{\rm Sr})$ are considered as perturbations to the Hamiltonian containing the kinetic operator and the electrostatic interactions. The states including SO are labeled according to the projection $|\Omega|$ of the total electronic angular momentum on the molecular axis [Hund's case (c)]. For the former asymptote, the $|\Omega| = 3/2$ Hamiltonian matrix (including electrostatic interaction and SO) reduces to a single element $W_{\rm so}^{\rm Rb}(|\Omega| = 3/2) = V((1)^2\Pi) + 2A^{\rm Rb}$, where $A^{\rm Rb} = \Delta_{\rm fs}^{\rm Rb}/3$, while the matrix for $|\Omega| = 1/2$ reads

$$W_{\rm so}^{\rm Rb}\left(|\Omega| = \frac{1}{2}\right) = \begin{pmatrix} V((2)^2\Sigma^+) & \sqrt{2}A^{\rm Rb} \\ \sqrt{2}A^{\rm Rb} & V((1)^2\Pi) + A^{\rm Rb} \end{pmatrix}. \quad (1)$$

For the latter dissociation limit, defining $A^{\rm Sr} = \Delta_{\rm fs}^{\rm Sr}/3$, the maximal value of $|\Omega|$ is 5/2, with a single matrix element $W_{\rm so}^{\rm Sr}(|\Omega| = 5/2) = V((1)^4\Pi) + A^{\rm Sr}$, while the matrices are, for $|\Omega| = 3/2$ and $|\Omega| = 1/2$,

$$W_{\rm so}^{\rm Sr}\left(|\Omega| = \frac{3}{2}\right) = \begin{pmatrix} V((2)^2\Pi) + \frac{2}{3}A^{\rm Sr} & \sqrt{\frac{1}{3}}A^{\rm Sr} & -\frac{\sqrt{2}}{3}A^{\rm Sr} \\ \sqrt{\frac{1}{3}}A^{\rm Sr} & V((1)^4\Sigma^+) & \sqrt{\frac{2}{3}}A^{Sr} \\ -\frac{\sqrt{2}}{3}A^{\rm Sr} & \sqrt{\frac{2}{3}}A^{\rm Sr} & V((1)^4\Pi) + \frac{1}{3}A^{\rm Sr} \end{pmatrix} \quad (2)$$

and

$$W_{\rm so}^{\rm Sr}\left(|\Omega| = \frac{1}{2}\right) = \begin{pmatrix} V((3)^2\Sigma^+) & \sqrt{\frac{8}{9}}A^{\rm Sr} & 0 & -\frac{1}{3}A^{\rm Sr} & \sqrt{\frac{1}{3}}A^{\rm Sr} \\ \sqrt{\frac{8}{9}}A^{\rm Sr} & V((2)^2\Pi) - \frac{2}{3}A^{\rm Sr} & \frac{1}{3}A^{\rm Sr} & -\frac{\sqrt{2}}{3}A^{\rm Sr} & 0 \\ 0 & \frac{1}{3}A^{\rm Sr} & V(^4\Sigma^+) & \sqrt{\frac{8}{9}}A^{\rm Sr} & \sqrt{\frac{2}{3}}A^{\rm Sr} \\ -\frac{1}{3}A^{\rm Sr} & -\frac{\sqrt{2}}{3}A^{\rm Sr} & \sqrt{\frac{8}{9}}A^{\rm Sr} & V((1)^4\Pi) - \frac{1}{3}A^{\rm Sr} & 0 \\ \sqrt{\frac{1}{3}}A^{\rm Sr} & 0 & \sqrt{\frac{2}{3}}A^{\rm Sr} & 0 & V((1)^4\Pi) - A^{\rm Sr} \end{pmatrix}. \quad (3)$$

The Hund's case (c) PECs $(N)\Omega$ including SO interaction are straightforwardly obtained by diagonalization of the full Hamiltonian involving these matrices at each R value (Fig. 3). The asymptote Rb $(5p\,^2P)$ + Sr $(5s^2\,^1S_0)$ is split in two asymptotes: Rb $(5p\,^2P_{1/2})$ + Sr $(5s^2\,^1S_0)$ and Rb $(5p\,^2P_{3/2})$ + Sr $(5s^2\,^1S_0)$ (hereafter referred to as the $^2P_{1/2}$ and $^2P_{3/2}$ asymptotes, in short), while the asymptote Rb $(5s\,^2S)$ + Sr $(5s5p\,^3P)$ is split in three asymptotes: Rb $(5s\,^2S_{1/2})$ + Sr $(5s5p\,^3P_0)$, Rb $(5s\,^2S_{1/2})$ + Sr $(5s5p\,^3P_1)$, and Rb $(5s\,^2S_{1/2})$ + Sr $(5s5p\,^3P_2)$ (hereafter referred to as the $^3P_0$, $^3P_1$, and $^3P_2$ asymptotes, in short). A single $\Omega = 1/2$ PEC is correlated to the $^3P_0$ asymptote, and two PECs to the $^3P_1$ and $^3P_2$ asymptotes. Similarly, a single $\Omega = 3/2$ PEC is correlated to the $^3P_1$ asymptote, and two PECs to the $^3P_2$ asymptote. The equilibrium distances for excited-state PECs are still smaller than the one of the ground state, except for the $(8)1/2$ and $(3)\frac{3}{2}$ PECs almost identical to the $(1)^4\Sigma^+$ PEC. The crossings in the Hund's case (a) PECs become avoided crossings in the Hund's case (c).

We display in Table II the corresponding fundamental spectroscopic constants, as they are provided in several other publications [32,34]. As expected from Fig. 2, the equilibrium distances R_e and the harmonic constants ω_e are those of the states without SO, as the avoided crossings occur far from R_e. The dissociation energies are significantly changed, reflecting the magnitude of the atomic SO splittings. As already noted, our results are in good agreement with those of Ref. [32]. In contrast, significant differences are found with the work of Ref. [34], in particular for the well depth and for the ω_e constant. In the latter work, the authors considered the relativistic Dirac-Coulomb Hamiltonian where the electronic spin and consequently the related R-dependent relativistic interactions are explicitly accounted for under a four-component framework, as initially developed in Ref. [39], so that the SO interaction is included in a nonperturbative way. But they used a basis set which is significantly smaller than the one of Ref. [32], which thus may not be fully appropriate for excited states. Such differences in the PECs may also indicate a noticeable variation of the molecular SO coupling strength with the internuclear distance. Note that we have proved for the heaviest alkali-metal atom Fr [40] that an electronic structure calculation including only the scalar relativistic term (as

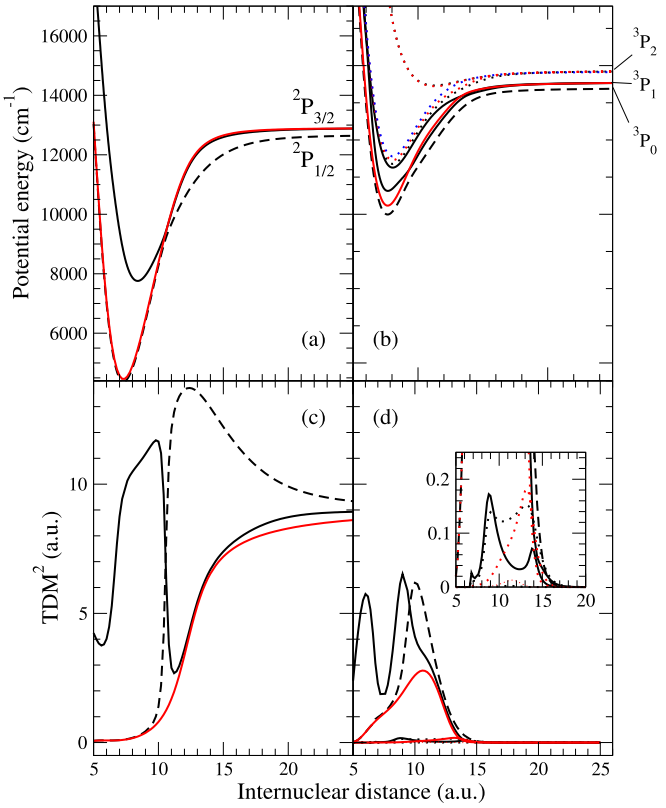

FIG. 3. RbSr potential-energy curves of excited states including spin-orbit interaction as described in the text [panels (a) and (b)], and corresponding effective squared transition dipole moments (TDM^2) from the $X\,^2\Sigma^+$ ground state towards the states correlated to $P_{1/2,3/2}$ [panel (c)] and to $^3P_{0,1,2}$ [panel (d)]. The PECs for $\Omega = 1/2,\ 3/2$, and $5/2$ are drawn in black, red (light gray), and blue (dark gray), respectively. Solid lines: states correlated to $^2P_{3/2}$ [(a) and (c)] and to $^3P_1$ [(b) and (d)]. Dashed lines: states correlated to $^2P_{1/2}$ [(a) and (c)] and to $^3P_0$ [(b) and (d)]. Dotted lines: states correlated to $^3P_2$ [(b) and (d)]. The inset is a zoom on the TDM^2 for the (6) $\frac{1}{2}$, (7) $\frac{1}{2}$, and (3) $\frac{3}{2}$ states.

performed here) yields satisfactory electronic atomic orbitals even for such a heavy species.

In Fig. 3 we also displayed the R-dependent quantity labeled with effective squared transition dipole moment (TDM^2), representing, for each molecular state $(N)\Omega$, the linear combination of the squared R-dependent TDMs of Fig. 1 associated with the transitions from the ground state toward the states involved in $(N)\Omega$. The weights of this combination are the squared components of the eigenvector associated with $(N)\Omega$. It should be noted that this quantity is not the one to consider for actually computing transition probabilities, i.e., it should not be used in an integration over R weighted by a pair of radial vibrational wave functions. Therefore, the TDM^2 quantities, referred to as "effective squared TDM" for convenience, only provide a qualitative description of the actual mixture of SO-free states composing $(N)\Omega$, by comparison between Fig. 3 and Fig. 1. As expected, our results for the TDM^2 quantities are very similar to those of Ref. [32]. This representation of the TDMs allows us to point out some features that have an impact on PA. First, the avoided crossings between PECs induce crossings between TDM curves due to the abrupt change of the nature of the electronic states. At short range, the (2) $\frac{1}{2}$ state [the (3) $\frac{1}{2}$ state] is mainly composed of (2) $^2\Pi$ state [(1) $^2\Sigma^+$ state]. This results in a high value for the former and a low value for the latter. The $^2\Pi$ state composition of the (1) $\frac{3}{2}$ state is also clear. For the transitions to Rb$(5s\,^2S_{1/2})$ + Sr$(5s5p\,^3P_{0,1,2})$ molecular states, the main characteristic is the nonzero value for (6) $\frac{1}{2}$, (7) $\frac{1}{2}$, and (8) $\frac{1}{2}$ states. Even if they are composed of quartet state at short range, the mixture with doublet states due to the spin-orbit interaction implies nonzero values at larger distance. At short range, we can also notice that the (4) $\frac{1}{2}$ and (2) $\frac{1}{2}$ states are mainly composed of (2) $^2\Pi$ state, while the (5) $\frac{1}{2}$ state is mainly composed of the (3) $^2\Sigma^+$ state.

III. PHOTOASSOCIATION OF ^{87}Rb^{84}Sr MOLECULES

A. Methodology

The photoassociation rate coefficients (in cm^{3}s^{-1}) toward a vibrational level v' of an excited electronic state e, at low laser intensity I, of a ^{87}Rb^{84}Sr pair colliding in the X ground state with relative energy $E = k_BT$, is computed according to the perturbative approach reported in Ref. [41]:

$$K_{PA}(X \to e, v'; T, I) = \frac{4\pi^{3/2}}{h\epsilon_0 c}\left(\frac{3}{2}\right)^{3/2}\lambda_{th}^3 \times I\left|\left\langle\phi^e_{v'}\middle|\mu_{eg}\middle|u^X_\ell(E)\right\rangle\right|^2, \quad (4)$$

where $\lambda_{th} = \sqrt{\frac{h^2}{3\mu k_B T}}$ is the de Broglie thermal wavelength of the atom pair with reduced mass μ, I is the intensity of the photoassociation laser, $\phi^e_{v'}(R)$ is the vibrational wave function of the photoassociated level v', $u^X_\ell(k_BT, R)$ is the continuum wave function of the colliding pair assuming a rotational quantum number (partial wave) ℓ, and $\mu_{eg}(R)$ is the R-dependent transition dipole moment between the $g \equiv X$ and e electronic states. For simplicity, we have considered an s-wave collisional regime ($\ell = 0$). The values of $I = 10\,\mathrm{W/cm^2}$ and $T = 5.5\,\mu\mathrm{K}$ are typical of the ongoing experiment [23], and are within the limits of validity of Eq. (4), namely in the linear regime for I, and for a nondegenerate quantum gas. This photoassociation rate coefficient is defined by the following kinetic equation:

$$\frac{d\rho^{e,v'}_{RbSr}}{dt} = K_{PA}\rho_{Rb}\rho_{Sr}, \quad (5)$$

where $\rho^{e,v'}_{RbSr}$ is the molecular density in the vibrational level v' of the excited electronic state e. ρ_{Rb} and ρ_{Sr} are the atomic densities of rubidium and strontium, respectively.

All radial wave functions are calculated with the MFGH method in the conditions previously specified. The continuum and vibrational levels of the $X\,^2\Sigma^+$ ground state are described in a single-channel representation; the wave functions (normalized to unity) describing levels of the continuum are renormalized in energy at the end of the calculation by dividing the wave function by the square root of the level density [42]. The vibrational wave functions of the ^{87}Rb^{84}Sr excited electronic states coupled by SO interaction are obtained from a multichannel representation according to Eqs. (1)–(3), and are therefore linear combinations of the related Hund's case

TABLE II. Main spectroscopic constants of the $^{87}Rb^{84}Sr$ electronic states including spin-orbit interaction, as compared to other published data. The corresponding dissociation limits are also indicated for the sake of clarity.

	FCI(ECP+CPP) [30]			KR-MRCI [34]			MCSCF-MRCI [32]		
Asymptote (state)	R_e (a_0)	D_e (cm^{-1})	ω_e (cm^{-1})	R_e (a_0)	D_e (cm^{-1})	ω_e (cm^{-1})	R_e (a_0)	D_e (cm^{-1})	ω_e (cm^{-1})
$Rb(5p\,^2P_{1/2}) + Sr(5s^2\,^1S_0)$									
(2) $\Omega = \frac{1}{2}$	7.30	8283.9	80.12	7.27	7883.09	85.73	7.43	8569.0	79.6
$Rb(5p\,^2P_{3/2}) + Sr(5s^2\,^1S_0)$									
(3) $\Omega = \frac{1}{2}$	8.39	5136.41	59.04	8.39	4683.56	58.43	8.56	5252.3	58.7
(1) $\Omega = \frac{3}{2}$	7.31	8439.8	79.50	7.29	7957.31	87.18	7.41	8727.6	80.4
$Rb(5s\,^2S_{1/2}) + Sr(5s5p\,^3P_0)$									
(4) $\Omega = \frac{1}{2}$	7.66	4234.40	68.85				7.82	4202.3	64.1
$Rb(5s\,^2S_{1/2}) + Sr(5s5p\,^3P_1)$									
(5) $\Omega = \frac{1}{2}$	7.69	3635.19	65.77				7.94	3436.2	52.4
(6) $\Omega = \frac{1}{2}$	8.06	2851.68	57.41						
$Rb(5s\,^2S_{1/2}) + Sr(5s5p\,^3P_2)$									
(7) $\Omega = \frac{1}{2}$	8.03	3112.45	57.63						
(8) $\Omega = \frac{1}{2}$	11.27	476.41	20.57						
$Rb(5s\,^2S_{1/2}) + Sr(5s5p\,^3P_1)$									
(2) $\Omega = \frac{3}{2}$	7.66	4129.30	68.34				7.82	4107.4	64.5
$Rb(5s\,^2S_{1/2}) + Sr(5s5p\,^3P_2)$									
(3) $\Omega = \frac{3}{2}$	8.06	2990.04	57.64						
(4) $\Omega = \frac{3}{2}$	11.30	501.73	21.05						
(1) $\Omega = \frac{5}{2}$	8.06	2990.04	56.98						

(a) electronic states weighted by the radial wave functions $\phi^e_{v'^2\Sigma}$ and $\phi^e_{v'^2\Pi}$. The squared matrix elements of the transition dipole moment $\mu_{eg}(R)$ involve the contributions of the $^2\Sigma^+$ and $^2\Pi$ components of the coupled excited electronic states as

$$\left|\langle\phi^e_{v'}|\mu_{eg}|u^X_0(E)\rangle\right|^2 = \left|\langle\phi^e_{v',^2\Sigma}|\mu_{^2\Sigma X}|u^X_0(E)\rangle\right|^2 + \left|\langle\phi^e_{v',^2\Pi}|\mu_{^2\Pi X}|u^X_0(E)\rangle\right|^2, \quad (6)$$

where the TDM functions $\mu_{^2\Sigma X}(R)$ and $\mu_{^2\Pi X}(R)$ are those displayed in Fig. 1. This equation is valid in the case of unpolarized light in the laboratory frame.

Two cases are of relevance for our study. First, the Sr intercombination transition is used in ongoing experiments devoted to the formation of the quantum degenerate mixture of strontium and rubidium atoms [31]. Therefore, we have studied the photoassociation close to the $^{87}Rb(5s\,^2S_{1/2}) + {}^{84}Sr(5s5p\,^3P_{0,1,2})$ asymptotes. However, PA will proceed in a very different way if it is implemented for laser frequencies close to the Rb dipole-allowed transition, namely, exploring bound levels close to the $^{87}Rb(5p\,^2P_{1/2,3/2}) + {}^{84}Sr(5s^2\,^1S_0)$ asymptotes, as investigated theoretically in Ref. [34].

It is worthwhile to emphasize the importance of accounting for the R dependence of the TDM functions in the PA rate coefficients, which is not considered in Ref. [34]. For this purpose, it is convenient to express the squared TDMs of Eq. (6) as the product of the squared overlap between radial wave functions (or Franck-Condon factors, FCF) and the values of electronic transition dipole moment at the outer turning point R_C of $\phi^e_{v'\Lambda}$ for the corresponding Λ excited electronic state

$$\left|\langle\phi^e_{v'\Lambda}|\mu_{eg}|u^X_0(E)\rangle\right|^2 = \mu^2_{eg}(R_C)\left|\langle\phi^e_{v'\Lambda}|u^X_0(E)\rangle\right|^2. \quad (7)$$

The general trend of the squared TDMs is illustrated in Fig. 4 for the (4) $\frac{1}{2}$ and the (2) $\frac{1}{2}$ states, respectively correlated to $^{87}Rb(5s\,^2S_{1/2}) + {}^{84}Sr(5s5p\,^3P_0)$ and to $^{87}Rb(5p\,^2P_{1/2}) + {}^{84}Sr(5s^2\,^1S_0)$. The squared TDMs have similar magnitude over most of the energy range of the potential wells, like the corresponding electronic transition dipole moments in the molecular range ($R < 12$ a.u. typically; see Fig. 1). Their behavior is very similar to the FCF one. Close to the $^{87}Rb(5s\,^2S_{1/2}) + {}^{84}Sr(5s5p\,^3P_0)$ asymptote, the squared TDM vanishes as $\mu^2_{eg}(R_C)$, while the FCFs increase. Therefore, the FCFs are not anymore representative of the variation of the squared TDMs. This is in striking contrast with PA close to the $^{87}Rb(5p\,^2P_{1/2}) + {}^{84}Sr(5s^2\,^1S_0)$ limit, for which the squared TDMs and the FCFs exhibit similar patterns. In conclusion, the use of FCFs for simulating the PA spectra must be made carefully, particularly in the case of forbidden atomic transitions. This decomposition of squared TDMs will also be useful when analyzing the PA spectra in the next section.

Ultracold molecules are stabilized by RE of the photoassociated molecules. For simplicity we assume, like in Ref. [41], that the RE probability is given by $\sum_{v''} |\langle\phi^e_{v'}(R)|\phi^g_{v'',g}(R)\rangle|^2$, involving only the components λ of the excited electronic state $|e\rangle$ which can reach the X state by a dipole-allowed transition.

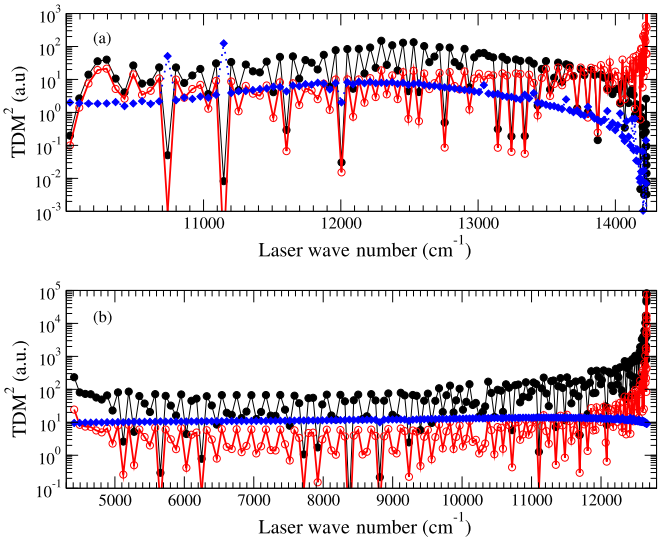

FIG. 4. Squared dipole matrix element for (a) the (4) $\frac{1}{2}$ levels correlated to ^{87}Rb$(5s\,^2S_{1/2}) + {}^{84}Sr(5s5p\,^3P_0)$, and (b) the (2) $\frac{1}{2}$ levels correlated to ^{87}Rb$(5p\,^2P_{1/2}) + {}^{84}Sr(5s^2\,^1S_0)$, as a function of the PA laser wave number. Black lines with closed circles: squared TDM from Eq. (6). Red (light gray) lines with open circles: squared overlap (FCF) between the radial wave functions involved in the PA rate coefficient. Blue (dark gray) dashed lines with losanges: squared TDM at the outer turning point R_C of the radial wave function of the photoassociated level.

The resulting UMF rate coefficient is written as

$$K_{\rm mol}^{v'} = K_{PA}^{v'} \sum_{v''} \left|\langle \phi_{v'}^{e} | \phi_{v''}^{g} \rangle\right|^2. \tag{8}$$

Note that Eq. (8) should be employed with care in the case of PA spectra close to the ^{87}Rb$(5s\,^2S_{1/2}) + {}^{84}Sr(5s5p\,^3P_{0,1,2})$ asymptotes as the TDM vanishes at large distances. It is actually more interesting to focus on the vibrational distribution in the ground-state levels after RE, which is more sensitive to the R variation of the electronic TDMs than the total UMF rate coefficient. We express the probability $P(v'' \leftarrow v')$ of a ground-state level v'' to be populated after RE from the photoassociated level v' as

$$P(v'' \leftarrow v') = \frac{\left|\langle \phi_{v'}^{e} | \mu_{eg} | \phi_{v''}^{g} \rangle\right|^2}{\sum_{v''} \left|\langle \phi_{v'}^{e} | \mu_{eg} | \phi_{v''}^{g} \rangle\right|^2}. \tag{9}$$

B. ^{87}Rb$(5s\,^2S_{1/2}) + {}^{84}Sr(5s5p\,^3P_{0,1,2})$ dissociation limit

PA rate coefficients for the five $\Omega = \frac{1}{2}$ states are shown on Fig. 5. For each potential, the analysis of these PA spectra could be divided in three parts: deeply bound levels, intermediate levels, and levels close to the asymptotes. For the deeply bound levels, the PA rate coefficient depends on their main composition of Hund's case (a) states. The most important values are obtained for (4) $\frac{1}{2}$ and (5) $\frac{1}{2}$ that are composed by (2) $^2\Pi$ and (3) $^2\Sigma^+$ states, respectively. Some of these deeply bound levels of (4) $\frac{1}{2}$ and (5) $\frac{1}{2}$ have a PA rate coefficient with only one order of magnitude less than the largest ones. These high values can be explained by the relative position of the (4) $\frac{1}{2}$ and (5) $\frac{1}{2}$ potential wells with respect to the ground-state

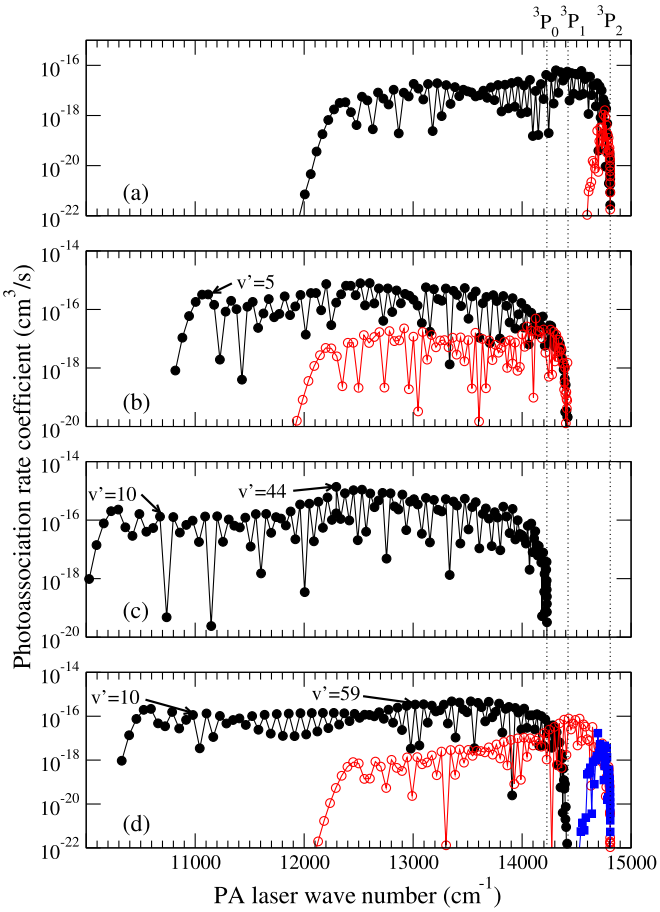

FIG. 5. Photoassociation rate coefficients for ^{87}Rb^{84}Sr levels as a function of the PA laser wave number, for states correlated to the ^{87}Rb$(5s\,^2S_{1/2}) + {}^{84}Sr(5s5p\,^3P_{0,1,2})$ dissociation limit. (a) (7) $\frac{1}{2}$ in black lines (closed circles), and (8) $\frac{1}{2}$ in red (open circles). (b) (5) $\frac{1}{2}$ in black (closed circles) and (6) $\frac{1}{2}$ in red (open circles). (c) (4) $\frac{1}{2}$ in black (closed circles). (d) (2) $\frac{3}{2}$ in black (closed circles), (3) $\frac{3}{2}$ in red (open circles), and (4) $\frac{3}{2}$ in blue (closed squares). In gray scale version, red is light gray and blue is dark gray.

one that favors the contribution of the distances at the inner turning point of the ground state in the PA rate coefficient.

The intermediate levels have the largest PA rate coefficients. This comes from the competition between the FCFs and the value of TDMs at the outer turning point as illustrated on Fig. 4. Due to their main proportion of (2) $^2\Pi$ and (3) $^2\Sigma^+$ states, the largest rate coefficients are obtained with the states (4) $\frac{1}{2}$ and (5) $\frac{1}{2}$: $1.4 \times 10^{-15}\,\mathrm{cm^{-3}s^{-1}}$ at $12295.1\,\mathrm{cm^{-1}}$ ($v' = 44$) and $5.4 \times 10^{-16}\,\mathrm{cm^{-3}s^{-1}}$ at $12601.3\,\mathrm{cm^{-1}}$ ($v' = 36$), respectively. For the (6) $\frac{1}{2}$, (7) $\frac{1}{2}$, and (8) $\frac{1}{2}$ states, the PA rate coefficients significantly increase, due to the admixture of doublet states in addition to the quartet component at large interatomic separation, while remaining quite small.

Finally, close to the asymptotes, the PA rate coefficients significantly drop down for all states. For example at a detuning around $0.15\,\mathrm{cm^{-1}}$, the PA rate coefficients are $7.2 \times 10^{-20}\,\mathrm{cm^{-3}s^{-1}}$ and $2.7 \times 10^{-22}\,\mathrm{cm^{-3}s^{-1}}$ for the (4) $\frac{1}{2}$ and (5) $\frac{1}{2}$ states, respectively. Therefore, PA already appears as a challenge close to the asymptote. New experimental results for PA in ^{84}Rb^{87}Sr are available [23]. In particular, the authors

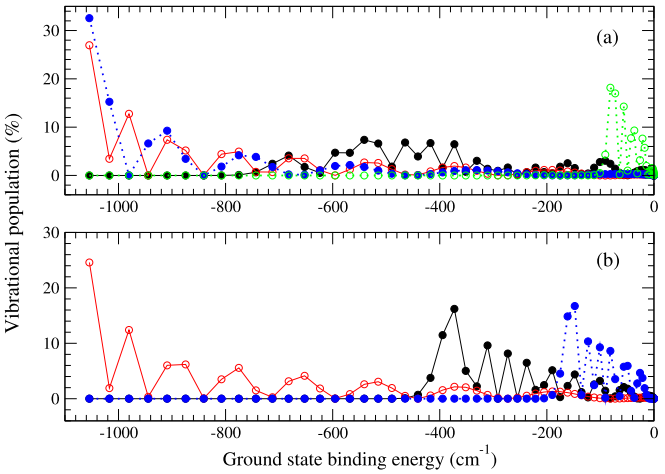

FIG. 6. Distribution of vibrational populations (displayed as percentage) of the ultracold ^{87}Rb^{84}Sr molecules created after spontaneous emission from several photoassociated levels of the (4) $\frac{1}{2}$, (5) $\frac{1}{2}$, and (2) $\frac{3}{2}$ states. (a) The $v' = 44$ (black line with closed circles), $v' = 10$ (red line with open circles), and $v' = 129$ (green line with open circles) levels of (4) $\frac{1}{2}$ and the $v' = 5$ (blue dashed line with closed circles) level of (5) $\frac{1}{2}$. (b) The $v' = 59$ (black line with closed circles), $v' = 10$ (red line with open circles), and $v' = 124$ (blue dashed line with closed circles) levels of (2) $\frac{3}{2}$. In gray scale version, red is intermediate gray, blue is dark gray, and green is light gray.

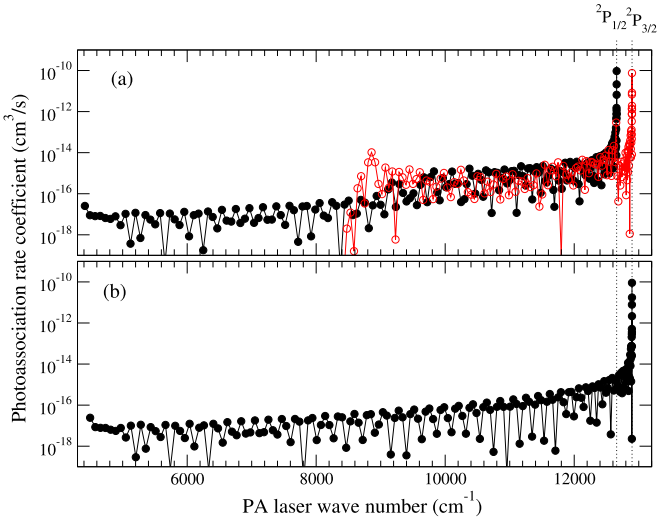

FIG. 7. Photoassociation rate coefficients as function of the PA laser wave number for the levels of (a) the (2) $\frac{1}{2}$ (black line with full circles) and (3) $\frac{1}{2}$ states [red (light gray) lines with empty circles] and (b) the (1) $\frac{3}{2}$ state, correlated to the Rb($5p\,^2P_{1/2,3/2}$) + Sr($5s^2\,^1S_0$) dissociation limit.

report difficulties to observe PA close to the ^{87}Rb($5s\,^2S_{1/2}$) + ^{84,87}Sr($5s5p\,^3P_1$) asymptote, and measure small photoassociation rate coefficients. Such low rate coefficients are consistent with our calculations.

The results for the $\frac{3}{2}$ state are rather similar [Fig. 5(d)]. The maximal PA rate coefficient [4.7×10^{-16} cm^{-3} s^{-1} for a detuning of 13018.32 cm^{-1} ($v' = 59$)] is found for (2) $\frac{3}{2}$, mainly composed of doublet states. Close to the asymptote, they also become rather low, remaining for (4) $\frac{3}{2}$ of the same order of magnitude as in the $\frac{1}{2}$ states.

The computed energy variations of the UMF rate coefficients are found very similar to those of the PA rate coefficients and are displayed in the Appendix for the sake of conciseness. Using Eq. (8), we find that the sum of squared overlaps in Eq. (8) decreases for (4) $\frac{1}{2}$ and (5) $\frac{1}{2}$, while it increases for (6) $\frac{1}{2}$ and (7) $\frac{1}{2}$, due to the admixture of doublet and quartet states as already explained for the PA rate coefficients. However, over the explored energy range, this sum has always the same magnitude and does not affect the energy pattern of the UMF rate coefficients with respect to the PA ones. The vibrational distributions in the ground-state levels [see Eq. (9)] are displayed in Fig. 6 for few typical photoassociated levels v': deeply bound levels [$v' = 5$ of (4) $\frac{1}{2}$, $v' = 10$ of (5) $\frac{1}{2}$, and $v' = 11$ of (2) $\frac{3}{2}$], intermediate levels [$v' = 44$ of (4) $\frac{1}{2}$ and $v' = 59$ of (2) $\frac{3}{2}$] that have the largest PA rate coefficients, and the last bound levels [$v' = 129$ of (4) $\frac{1}{2}$ and $v' = 124$ of (2) $\frac{3}{2}$]. The deeply bound levels can yield a main fraction of the population in the ground-state $v'' = 0$ level, as it can be expected from the favorable relative position of the minimum of the corresponding potential well in the excited state and in the ground state. The levels with the largest PA rate coefficients [in the (4) $\frac{1}{2}$ and the (2) $\frac{3}{2}$ states] yield a population spread over numerous ground-state vibrational levels, with no specific emergence of a particular level [a maximum population being found, however, for levels $v'' = 16$ ($E_{16} = -541$ cm^{-1}) and $v'' = 23$ ($E_{23} = -372$ cm^{-1}), respectively]. Finally, when PA is performed close to the asymptote, different levels with binding energies lower than 200 cm^{-1} are populated. The populations of the last bound levels of the ground state vanish as a consequence of the vanishing TDMs at large distance.

C. Rb($5p\,^2P_{1/2,3/2}$) + Sr($5s^2\,^1S_0$) dissociation limit

The computed PA rate coefficients for both $\Omega = \frac{1}{2}$ and $\Omega = \frac{3}{2}$ states are displayed in Fig. 7. For deeply bound levels, the PA rate coefficients are more important for (2) $\frac{1}{2}$ than for (3) $\frac{1}{2}$. This striking difference is at first sight counterintuitive. The levels of the (2) $\frac{1}{2}$ state composed mainly of the $^2\Pi$ (low value at short-range) state have larger PA rate coefficients than levels from (3) $\frac{1}{2}$ state composed mainly of $^2\Sigma^+$ (high value at short range). This is due to weak FCFs for the deeply bound levels of (3) $\frac{1}{2}$ state. Close to the asymptotes, PA rate coefficients quickly rise. The results are very similar to those obtained for the alkali-metal dimers, as the dominant role is given to the dipole-allowed Rb transition. In a classical view, PA takes place mostly at large interatomic distances, where the electronic TDM is large and where the overlap between the relevant radial wave functions is favored. This could be seen on Fig. 4(b). The rate coefficient magnitude is found similar to the one for Rb photoassociation [43]. The maximal values (10^{-10}–10^{-11} cm^{-3}s^{-1}) close to the dissociation limits are tedious to compare to experiment, as the cloud of cold atoms is strongly perturbed if the PA laser is tuned too close to the atomic resonance.

As previously, the UMF rate coefficient variations with the PA laser frequency are very similar to the ones of the PA rate coefficients (see the Appendix). The computed vi-

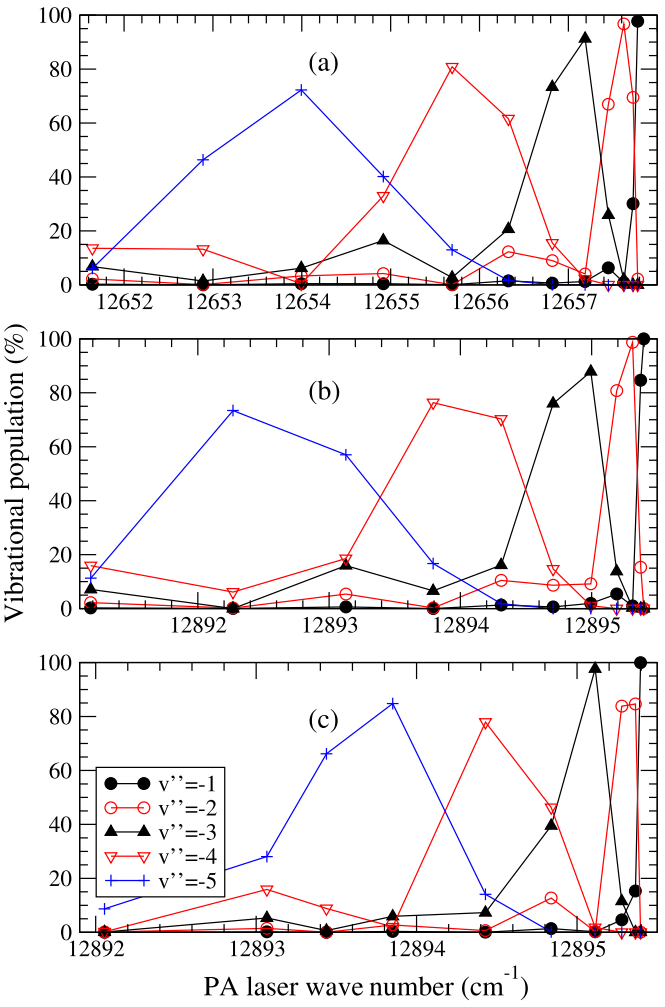

FIG. 8. Distribution of vibrational populations (displayed as percentage) of the five uppermost vibrational levels (labeled as $v'' = -1, -2, -3, -4, -5$ for convenience) of the ^{87}Rb^{84}Sr ground state, generated after spontaneous emission from the photoassociated levels of the (2) $\frac{1}{2}$, (3) $\frac{1}{2}$, and (1) $\frac{3}{2}$ states [panels (a), (b), and (c), respectively] identified by the PA laser wave number.

brational distributions generated by the photoassociated levels are actually quite remarkable, as illustrated in Fig. 8. They reflect an almost diagonal Franck-Condon matrix, namely each photoassociated level almost populates a single ground-state level: for instance, the last-but-one ground-state level (noted $v'' = -1$ for convenience) is populated at 97.75% by the last-but-one (also noted $v' = -1$ for convenience) level of (2) $\frac{1}{2}$, at 99.98% with the $v' = -1$ level of (3) $\frac{1}{2}$ and at 99.94% of (1) $\frac{3}{2}$. The purity of the relaxation process is worse when the detuning is increased. But, in any case, only weakly bound ground-state molecules could be efficiently created. Note that this situation has been also investigated in Ref. [34] based only on the FCFs, yielding results similar to ours.

IV. FORMATION OF ULTRACOLD WEAKLY BOUND ^{87}Rb ^{84}Sr MOLECULES BY A STIRAP TRANSFER IN A TIGHT OPTICAL TRAP

In the previous section, we have shown that the formation of RbSr ground-state molecules could be achieved by PA. However, the spontaneous emission induces two well-known drawbacks: the loss of atoms from the trap and a broad distribution of occupied vibrational levels. Even if this last point is minimized when PA is implemented with a laser frequency close to the dipole-allowed Rb transition (see Sec. III C), employing a coherent method avoiding spontaneous emission would decrease the loss of atoms. The most efficient method of coherent population transfer is the stimulated rapid adiabatic passage (STIRAP) method [44], relying on a proper choice of three energy levels, referred to as a Λ system. It allows the coherent population transfer between an initial level $|i\rangle$ and a final level $|f\rangle$ through a dark state involving an excited level $|e\rangle$. When the two-photon detuning δ (i.e., the difference between the laser frequencies addressing the $|i\rangle \rightarrow |e\rangle$ and $|e\rangle \rightarrow |f\rangle$ transitions) is zero, one of the instantaneous eigenstates of the Hamiltonian including the light is a coherent superposition of only $|i\rangle$ and $|f\rangle$ and is the so-called dark state. The transfer could be made without populating the intermediate level $|e\rangle$, thereby avoiding loss by spontaneous emission. The complete population transfer from $|i\rangle$ to $|f\rangle$ is achieved by the application of a pair of pump and dump pulses in a counterintuitive order. As the system must remain in the dark state during all of the process, the dynamics has to be adiabatic, thus imposing constraints on the corresponding Rabi frequencies $\Omega_{\rm pump}$ and $\Omega_{\rm dump}$: they must have the same order of magnitude and they must be sufficiently large to satisfy the condition $\Omega_{\rm pump,dump} T \gg \pi$, where T is the duration of the pulses.

The use of STIRAP in a PA experiment (i.e., without relying on Feshbach resonances) was previously investigated [45], revealing some difficulties due to the fact that the initial level belongs to a dissociation continuum, preventing the perfect creation of the dark state. One can overcome this drawback by placing the initial cold atoms in a tight optical trap (say, at a typical wavelength of 1064 nm), such that the motional states of the atom pair become quantized [26]. At ultracold temperature, the atoms occupy the lowest motional level of the trap. Therefore, the radial wave function of the atom pair should be localized at shorter distance and the FCFs with the bound levels of excited electronic states should increase.

The Hamiltonian describing two nonidentical atoms of mass m_1 and m_2 at positions $\vec{r}_1$ and $\vec{r}_2$ in an optical anharmonic trap with harmonic frequencies ω_1 and ω_2 felt by each atomic species is [46]

$$H_{\rm trap} = -\frac{\hbar^2}{2M}\Delta_{\rm com} + \frac{1}{2}M\omega_{\rm com}^2 R_{\rm com}^2 - \frac{\hbar^2}{2\mu}\Delta_R + \frac{1}{2}\mu\omega_R^2 R^2 + V(R) + \mu\Delta\omega\vec{R}_{\rm com}\cdot\vec{R} + V_{\rm anharm}, \quad (10)$$

with the total mass $M = m_1 + m_2$, the reduced mass $\mu = \frac{m_1 m_2}{M}$, the position of the center-of-mass $\vec{R}_{\rm c.m.} = \frac{m_1\vec{r}_1 + m_2\vec{r}_2}{M}$, the relative position vector $\vec{R} = \vec{r}_1 - \vec{r}_2$, and $\Delta\omega = \sqrt{\omega_1^2 - \omega_2^2}$. The first two terms represent the center-of-mass motion in the trap, with frequency $\omega_{\rm c.m.} = \sqrt{\frac{m_1\omega_1^2 + m_2\omega_2^2}{m_1 + m_2}}$. The next three terms describe the relative motion of the atom pair interacting through the potential $V(R)$, in the presence of a trapping potential of frequency $\omega_R = \sqrt{\frac{m_2\omega_1^2 + m_1\omega_2^2}{m_1 + m_2}}$. These two motions are in principle coupled by the anharmonic terms $V_{\rm anharm}$

of the trapping potential and by a dynamical term proportional to $R_{\mathrm{c.m.}} \cdot R$. The former can be safely neglected if we assume that the atoms are trapped in the lowest motional level. The latter depends on the differences of masses and polarizabilities that are almost the same in the present case. In our calculations, we have therefore neglected the coupling between the two motions, and worked with relative coordinates. We have taken the experimental trapping frequencies $2\pi \times 65\,\mathrm{kHz}$ for ^{84}Sr and $2\pi \times 110\,\mathrm{kHz}$ for ^{87}Rb [47]. The characteristic length of the relative motion in the trap is $a_\omega = \sqrt{\hbar/\mu\omega_{\mathrm{rel}}} = 969$ a.u., which is much larger than the scattering length. Therefore, the tight trap does not induce any significant modification of bound levels of the ground and excited molecular states. The eigenstates of H_{trap} for the ground and excited states of Fig. 3 as well as the transition matrix elements are computed with the MFGH method as in the previous sections. The main difference is that the radial wave functions of the trap states are now normalized to unity, as they are no longer continuum states.

The initial level $|i\rangle$ is taken as the first trap state. For the final level $|f\rangle$, we have chosen the vibronic ground-state level ($v'' = 0$). We have also examined the possibility to improve the STIRAP process toward another final level. The crucial element of the model is the choice of the best possible intermediate level $|e\rangle$ belonging to an excited electronic state. In an experiment, it is usually required to identify pump and dump transitions with similar Rabi frequencies and manageable amplitude. In the present model, we chose for simplicity a criterion independent from the experimental conditions: we look for pump and dump transitions with transition dipole moments ($|\mu_{ie}|^2 = |\langle\phi^e_{v_e}|\mu_{eg}|\phi_{\mathrm{trap}}\rangle|^2$ and $|\mu_{ef}|^2 = |\langle\phi^e_{v_e}|\mu_{eg}|\phi^g_{v_f}\rangle|^2$) of similar magnitude. We thus pin down a domain of possible transitions that could be further explored by experimentalists depending on the characteristics of the used lasers.

For the transfer toward $|f\rangle \equiv |v'' = 0\rangle$ via the states $|e\rangle$ correlated to $^{87}\mathrm{Rb}(5s\,^2S_{1/2}) + {}^{84}\mathrm{Sr}(5s5p\,^3P_{0,1,2})$ [Fig. 9(a)], the squared TDME curves for the pump and dump transitions cross each other twice, around $12000\,\mathrm{cm}^{-1}$ and $14500\,\mathrm{cm}^{-1}$ with very weak magnitudes (10^{-9}–10^{-10} a.u.). A similar conclusion holds for the transfer via the levels $|e\rangle$ belonging to states correlated to $\mathrm{Rb}(5p\,^2P_{1/2,3/2}) + \mathrm{Sr}(5s^2\,^1S_0)$, where the two curves cross once around $8500\,\mathrm{cm}^{-1}$ [Fig. 9(c)] at a low magnitude (10^{-9} a.u.). These statements actually reflect the behavior of the corresponding PA rate coefficients of Figs. 5 and 7. While providing a discrete level for the initial state for STIRAP, the choice of a confined trap level for the pump step does not significantly improve the magnitude of the squared TDMs compared to the conventional PA starting from a real continuum state.

Panels (b) and (d) in Fig. 9 illustrate another possible way to progress on the way to the creation of ultracold ^{87}Rb^{84}Sr molecules. We have calculated the TDMs involved in the transfer from the initial trap state toward the $v'' = -3$ level of the ^{87}Rb^{84}Sr ground state, leading to a contrasted result: while the STIRAP transfer does not seem to be possible via $|e\rangle$ levels belonging to states correlated to $^{87}\mathrm{Rb}(5s\,^2S_{1/2}) + {}^{84}\mathrm{Sr}(5s5p\,^3P_{0,1,2})$ [Fig. 9(b)], it appears doable via $|e\rangle$ levels close to the $\mathrm{Rb}(5p\,^2P_{1/2,3/2}) + \mathrm{Sr}(5s^2\,^1S_0)$ dissociation limit [see the extreme right part of Fig. 9(d), for which the squared TDMs for the pump and dump transitions can reach similar values up to 10^{-5} a.u.]. In fact, the five uppermost bound levels could be populated by a STIRAP with an intermediate level close to the asymptotes $^2P_{1/2}$ or $^2P_{3/2}$ (see Table III). As expected, the STIRAP is more tedious for more deeply bound final levels. In conclusion, the STIRAP method in a tight trap can create only weakly bound ^{87}Rb ^{84}Sr ground-state molecules, just like PA or magnetoassociation based on Feshbach resonances.

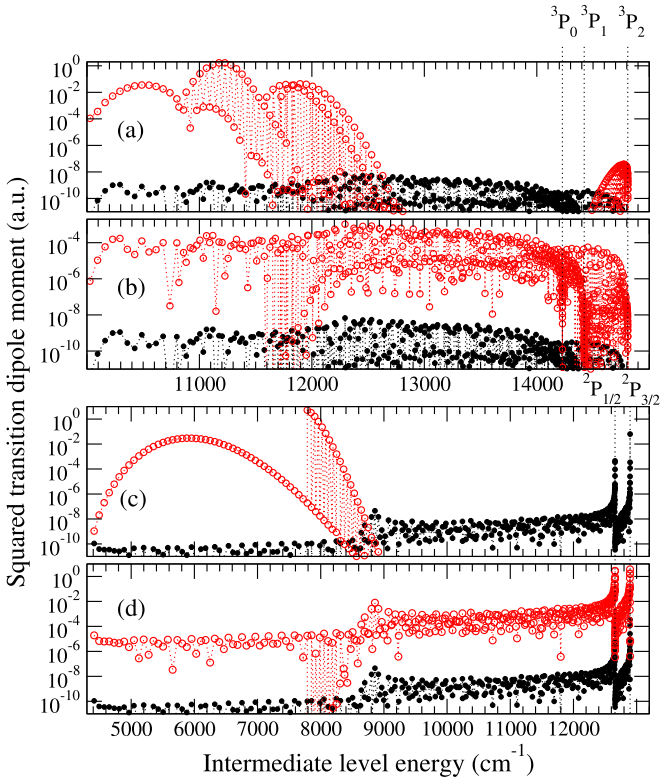

FIG. 9. Squared matrix elements of the transition dipole moment (squared TDMs in short) relevant for the formation of ^{87}Rb^{84}Sr molecules with STIRAP, starting from an atom pair confined in the lowest motional level of a tight optical trap (see text for details), as a function of the excitation energy of the chosen intermediate level $|e\rangle$ (with respect to the ground-state asymptote energy). Pump transitions: black lines with closed circles; dump transitions: red (light gray) lines with open circles. Panels (a) and (c) [(b) and (d)] correspond to the final level $|f\rangle \equiv v'' = 0$ ($|f\rangle \equiv v'' = -3$) of the electronic ground state. The levels $|e\rangle$ belong to all electronic states $\Omega = \frac{1}{2}$ correlated to $^{87}\mathrm{Rb}(5s\,^2S_{1/2}) + {}^{84}\mathrm{Sr}(5s5p\,^3P_{0,1,2})$ [panels (a) and (b)] and to $\mathrm{Rb}(5p\,^2P_{1/2}) + \mathrm{Sr}(5s^2\,^1S_0)$ [panels (c) and (d)].

V. POPULATION TRANSFER FROM WEAKLY BOUND ^{87}Rb ^{84}Sr GROUND-STATE MOLECULES TO THE ROVIBRATIONNAL GROUND STATE

In the past two sections, we have shown that the formation of weakly bound ^{87}Rb ^{84}Sr ground-state molecules is achievable by PA and by STIRAP in a tight trap. A second STIRAP step could then be implemented to transfer these molecules into the lowest level of the ground state. Such a double STIRAP sequence has already been applied for ultracold Cs_2 molecules [48]. We have looked for an optimal STIRAP

TABLE III. Characteristics of the optimal transitions for the STIRAP scheme in a tight trap via an intermediate level close to $Rb(5p\,^2P_{1/2}) + Sr(5s^2\,^1S_0)$. The initial level is the first trap state, with an energy of $5 \times 10^{-6}\,cm^{-1}$ (or about 150 kHz) above $Rb(5s\,^2S_{1/2}) + Sr(5s^2\,^1S_0)$. The final level of the ground state is labeled with negative index $\tilde{v}_f$ starting from the $Rb(5s\,^2S_{1/2}) + Sr(5s^2\,^1S_0)$ asymptote, with a binding energy E_f. The vibrational index v_e and binding energy E_e of several optimal intermediate levels are displayed. The energies E_{pump} and E_{dump} and the related squared transition dipole moments $|\mu_{ie}|^2$ and $|\mu_{ef}|^2$ of the pump and dump transitions are also reported. Numbers in parentheses hold for powers of 10.

$\tilde{v}_f$	−1	−2	−3	−4	−5
E_f (cm^{-1})	1.3 (−3)	2.58 (−2)	1.147 (−1)	3.112 (−1)	6.573 (−1)
v_e	161	201	199	198	197
	3 ($\frac{1}{2}$)	2 ($\frac{1}{2}$)	2 ($\frac{1}{2}$)	2 ($\frac{1}{2}$)	2 ($\frac{1}{2}$)
E_e (cm^{-1})	2.9 (−3)	2.0 (−3)	7.16 (−2)	1.755 (−1)	3.494 (−1)
E_{pump} (cm^{-1})	12895.4000	12657.7979	12657.7279	12657.6238	12657.4490
$\|\mu_{ie}\|^2$ (a.u.)	6.2 (−2)	4.5 (−4)	9.3 (−5)	2.8 (−6)	2.8 (−5)
E_{dump} (cm^{-1})	12895.4012	12657.8238	12657.8426	12657.9350	12658.1063
$\|\mu_{ef}\|^2$ (a.u.)	1.2 (0)	7.4 (−4)	2.3 (−4)	7.1 (−6)	2.5 (−5)

transfer starting from the five uppermost ground-state levels above, now labeled as $v_i = -1, -2, -3, -4, -5$. We have identified three efficient STIRAP paths in three different spectral zones, based upon the same criterion as above of the equality of the squared TDMs for the pump and dump transitions.

The first scheme relies on lowest bound levels of the 2 ($\frac{1}{2}$) state correlated to $Rb(5p\,^2P_{1/2}) + Sr(5s^2\,^1S_0)$, corresponding

TABLE IV. Characteristics of the optimal transition for STIRAP schemas. The final level is the rovibrational ground state ($v'' = 0$). The vibrational number and binding energy E_e are given for the intermediate level. The energies E_{pump} and E_{dump} and the related squared transition dipole moments $|\mu_{ie}|^2$ and $|\mu_{ef}|^2$ of the pump and dump transitions are also reported. Numbers in parentheses hold for powers of 10.

Initial level					
v_i	−1	−2	−3	−4	−5
E_i (cm^{-1})	1.3 (−3)	2.58 (−2)	1.147 (−1)	3.112 (−1)	6.573 (−1)
Final level					
v_f	0	0	0	0	0
E_f (cm^{-1})	1054.3406	1054.3406	1054.3406	1054.3406	1054.3406
First STIRAP scheme					
v_e [(2) $\Omega = \frac{1}{2}$]	4	4	5	6	6
E_e (cm^{-1})	7926.4524	7926.4524	7847.7908	7769.4210	7769.4210
E_{pump} (cm^{-1})	4731.3473	4731.3473	4810.3193	4889.0356	4889.0356
$\|\mu_{ie}\|^2$ (a.u.)	2.1 (−7)	1.7 (−6)	4.5 (−6)	1.2 (−5)	2.0 (−5)
E_{dump} (cm^{-1})	5785.6882	5785.6882	5864.3497	5942.7196	5942.7196
$\|\mu_{ef}\|^2$ (a.u.)	6.1 (−6)	6.1 (−6)	2.4 (−5)	7.6 (−5)	7.6 (−5)
Second STIRAP scheme					
v_e [(2) $\Omega = \frac{1}{2}$]	40	40	39	37	37
E_e (cm^{-1})	5275.7563	5275.7563	5344.3918	5482.5236	5482.5236
E_{pump} (cm^{-1})	7382.0436	7382.0687	7313.5220	7175.5865	7175.9330
$\|\mu_{ie}\|^2$ (a.u.)	2.5 (−7)	2.1 (−6)	1.4 (−6)	1.1 (−5)	1.9 (−5)
E_{dump} (cm^{-1})	8436.3843	8436.3843	8367.7488	8229.6170	8229.6170
$\|\mu_{ef}\|^2$ (a.u.)	1.8 (−6)	1.8 (−6)	3.8 (−6)	1.6 (−5)	1.6 (−5)
Third STIRAP scheme					
v_e [(5) $\Omega = \frac{1}{2}$]	16	15	15	15	15
E_e (cm^{-1})	2746.0037	2746.0131	2746.0131	2746.0131	2746.0131
E_{pump} (cm^{-1})	11675.2972	11626.3119	11626.4005	11626.5954	11626.9390
$\|\mu_{ie}\|^2$ (a.u.)	7.4 (−6)	2.0 (−5)	5.5 (−5)	1.1 (−4)	1.7 (−4)
E_{dump} (cm^{-1})	12414.0104	12362.3483	12362.3483	12362.3483	12362.3483
$\|\mu_{ef}\|^2$ (a.u.)	1.8 (−5)	9.8 (−5)	9.8 (−5)	9.8 (−5)	9.8 (−5)

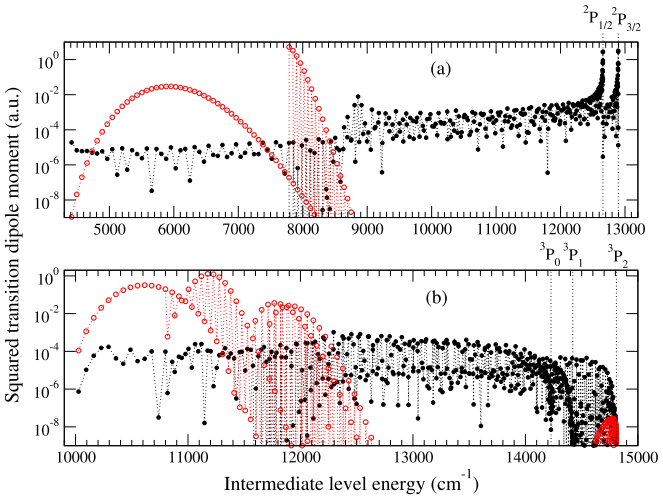

FIG. 10. Same as in Fig. 9 except different initial and final levels, $v'' = -3$ and $v'' = 0$, respectively. Panels (a) [(b)] correspond to STIRAP with intermediate levels belonging to all electronic states correlated to $\mathrm{Rb}(5p\,^2P_{1/2}) + \mathrm{Sr}(5s^2\,^1S_0)$ [$^{87}\mathrm{Rb}(5s\,^2S_{1/2}) + {}^{84}\mathrm{Sr}(5s5p\,^3P_{0,1,2})$].

to E_{pump} in the 4570–4890 cm^{-1} range and E_{dump} in the 5625–5945 cm^{-1} range [Table IV and Fig. 10(a)]. Despite a strong magnitude of the corresponding squared TDMs, that may not be the most practical frequencies to implement experimentally. As already noticed before, the possibility to use the lowest bound levels of the intermediate state comes from the relative position of PECs, and from the position of the inner turning point of the initial weakly bound vibrational wave function, located close to the equilibrium distance of excited states.

The second scheme relies on the intermediate levels of the same state, with levels that can be reached with E_{pump} in the 7175–7590 cm^{-1} range, inducing E_{dump} located in the 8230–8640 cm^{-1} range [Table IV and Fig. 10(a)]. This scheme is expected to be slightly less efficient than the previous one, but in a more accessible frequency domain for the STIRAP lasers. This solution involves the vibrational levels close to the avoided crossing between the $^2\Sigma^+$ and $^2\Pi$ states (see Fig. 1).

The third scheme involves levels of the 4 $(\frac{1}{2})$ state correlated to $\mathrm{Rb}(5s\,^2S_{1/2}) + \mathrm{Sr}(5s5p\,^3P_2)$ [Table IV and Fig. 10(b)], with E_{pump} in the 11200–11360 cm^{-1} range and E_{dump} in the 12255–12415 cm^{-1} range. This corresponds to levels with an energy close to the avoided crossing visible in Fig. 9. The efficiency of this STIRAP path seems to be the best of the three presented in this work. The advantage of this path is that a Ti:Sa laser could be used.

Chen *et al.* [34] have proposed another STIRAP path using the $v_e = 21$ level of the (2) $\frac{1}{2}$ state as the intermediate level, relying on a hypothesis different from ours: the selected intermediate level should be the one with the largest value for the product of the squared TDMs for the pump and dump transitions (reduced to FCFs in their paper). In the case (like the current situation) where the squared TDMs for the pump and the dump transitions are vastly different, this methodology implies very different laser intensities. The STIRAP path presented in our work would be more interesting if the intensity range of the pump and dump lasers are the same. On the other hand, if higher power could be used for the pump laser, the STIRAP path of Chen *et al.* [34] could be indeed appropriate.

VI. CONCLUSION

In this work, we have made a complete investigation about the possible ways to create ultracold $^{87}\mathrm{Rb}\,^{84}\mathrm{Sr}$ bosonic molecules in their rovibronic absolute ground state by all-optical methods. We have modeled the photoassociation of (^{87}Rb, ^{84}Sr) atom pairs close to two atomic transitions: the allowed $5s^2S_{1/2} \rightarrow 5p\,^2P_{1/2,3/2}$ Rb transition and the $5s^2\,^1S_0 \rightarrow 5s5p\,^3P_{0,1,2}$ Sr intercombination transition. As expected, the photoassociation spectra show opposite behaviors. In the former case, the photoassociation rate coefficients are very high close to the asymptote. In the latter case, the photoassociation rate coefficients are very low close to the asymptotes. The distributions of ground-state vibrational levels after spontaneous

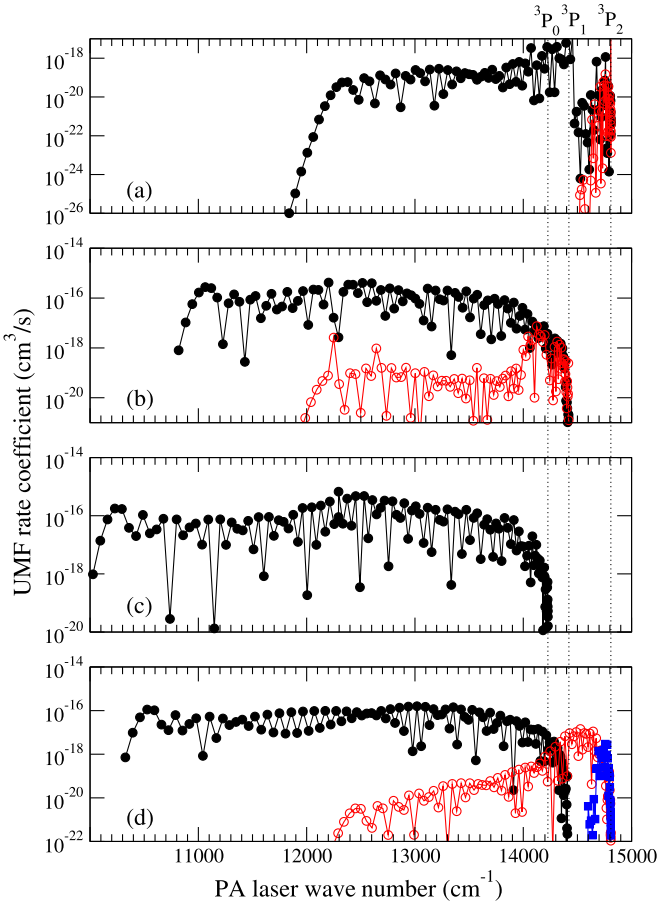

FIG. 11. Ultracold molecule formation rate coefficients for $^{87}\mathrm{Rb}^{84}\mathrm{Sr}$ levels as a function of the PA laser wave number, for states correlated to the $^{87}\mathrm{Rb}(5s\,^2S_{1/2}) + {}^{84}\mathrm{Sr}(5s5p\,^3P_{0,1,2})$ dissociation limit. (a) (7) $\frac{1}{2}$ in black lines (closed circles) and (8) $\frac{1}{2}$ in red (open circles). (b) (5) $\frac{1}{2}$ in black (closed circles) and (6) $\frac{1}{2}$ in red (open circles). (c) (4) $\frac{1}{2}$ in black (closed circles). (d) (2) $\frac{3}{2}$ in black (closed circles), (3) $\frac{3}{2}$ in red (open circles), and (4) $\frac{3}{2}$ in blue (closed squares). In gray scale version, red is light gray and blue is dark gray.

emission are also different. Mainly one vibrational level is populated in the former case, but this level is highly excited. In the latter case, the lowest rovibrational level of the ground state could be populated, but many other vibrational levels as well. Therefore, a further step of internal cooling is necessary to achieve a significant creation of ultracold RbSr molecules in their lowest rovibrational level.

We have then proposed to implement the formation of ultracold ^{87}Rb ^{84}Sr molecules by a STIRAP method in a tight trap. We found that a single STIRAP sequence to reach the lowest rovibrational ground-state level is tedious with moderate laser intensity. However, with an intermediate level close to the allowed $5s^2S_{1/2} \rightarrow 5p\,^2P_{1/2,3/2}$ Rb transition, a STIRAP scheme is possible for populating one of the five uppermost vibrational levels of the ground state. We then completed our study by modeling a further STIRAP sequence to efficiently transfer the population from these uppermost levels toward the lowest rovibrational ground-state level. Three STIRAP schemes have been identified in three different spectral zones.

Together with the recent spectacular experimental achievements of the Amsterdam group [23,25] revealing magnetic Feshbach resonances in RbSr and a description of the entire PEC of the RbSr ground state, the present work should help to progress toward the realization of a molecular sample of ultracold RbSr polar molecules. From our investigation it appears that, in contrast to the ongoing experiment, considering the possibility to use lasers close to the allowed $5s^2S_{1/2} \rightarrow 5p\,^2P_{1/2,3/2}$ Rb transition would probably be necessary to reach this objective.

ACKNOWLEDGMENTS

The authors are grateful to Alessio Ciamei, Florian Schreck, and the Amsterdam group for providing us with experimental results prior to publication. A.D. and O.D. acknowledge the support of the ANR BLUESHIELD (Grant No. ANR-ANR-14-CE34-0006) and the MesoLUM center for the computational resources. This work benefited from the scientific environment of the "Groupement de Recherches THEMS" (Grant No. GDR 3575) of CNRS.

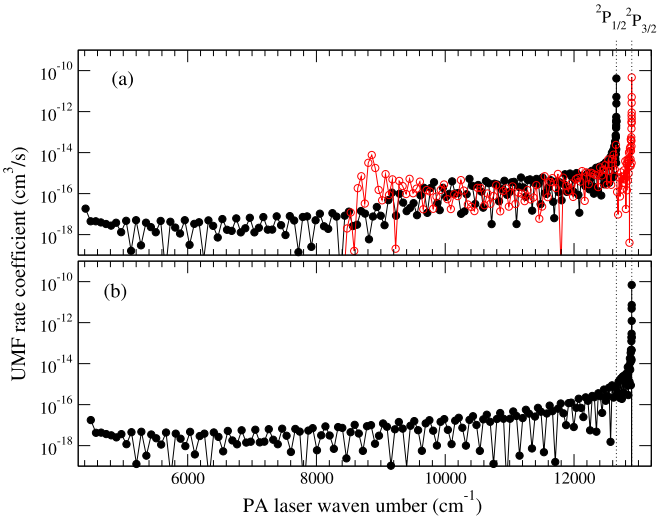

FIG. 12. Ultracold molecule formation rate coefficients as function of the PA laser wave number for the levels of the (a) (2) $\frac{1}{2}$ (black line with full circles) and (3) $\frac{1}{2}$ states [red (light gray) lines with empty circles] and (b) of the (1)$\frac{3}{2}$ state, correlated to the $\mathrm{Rb}(5p\,^2P_{1/2,3/2}) + \mathrm{Sr}(5s^2\,^1S_0)$ dissociation limit.

APPENDIX

In Figs. 11 and 12 we display the UMF rate coefficients corresponding to the situations treated in Sec. III. We recall that these rate coefficients are obtained with Eq. (7) which disregards the R-dependent TDM for the RE step. Therefore, these graphs are intended to yield a global illustration of the variation of the UMF rate coefficient with the detunings, while the calculation of the vibrational distributions of the ground-state molecules are indeed computed taking in account these TDMs [see Eq. (8)].

[1] J. T. Bahns, P. Gould, and W. Stwalley, J. Chem. Phys. **104**, 9689 (1996).
[2] L. D. Carr, D. DeMille, R. V. Krems, and J. Ye, New J. Phys. **11**, 055049 (2009).
[3] G. Quéméner and P. S. Julienne, Chem. Rev. **112**, 4949 (2012).
[4] M. Karra, K. Sharma, B. Friedrich, S. Kais, and D. Herschbach, J. Chem. Phys. **144**, 094301 (2016).
[5] K. Sharma and B. Friedrich, New J. Phys. **17**, 045017 (2015).
[6] A. Micheli, G. K. Brennen, and P. Zoller, Nat. Phys. **2**, 341 (2006).
[7] D. Comparat, C. Drag, B. L. Tolra, A. Fioretti, P. Pillet, A. Crubellier, O. Dulieu, and F. Masnou-Seeuws, Eur. Phys. J. D **11**, 59 (2000).
[8] C. Gabbanini, A. Fioretti, A. Lucchesini, S. Gozzini, and M. Mazzoni, Phys. Rev. Lett. **84**, 2814 (2000).
[9] H. R. Thorsheim, J. Weiner, and P. S. Julienne, Phys. Rev. Lett. **58**, 2420 (1987).
[10] K. M. Jones, E. Tiesinga, P. D. Lett, and P. S. Julienne, Rev. Mod. Phys. **78**, 483 (2006).
[11] J. Deiglmayr, A. Grochola, M. Repp, K. Mörtlbauer, C. Glück, J. Lange, O. Dulieu, R. Wester, and M. Weidemüller, Phys. Rev. Lett. **101**, 133004 (2008).
[12] M. Viteau, A. Chotia, M. Allegrini, N. Bouloufa, O. Dulieu, D. Comparat, and P. Pillet, Science **321**, 232 (2008).
[13] A. Wakim, P. Zabawa, M. Haruza, and N. P. Bigelow, Opt. Express **20**, 1683 (2012).
[14] I. Manai, R. Horchani, H. Lignier, P. Pillet, D. Comparat, A. Fioretti, and M. Allegrini, Phys. Rev. Lett. **109**, 183001 (2012).
[15] R. Beuc, M. Movre, T. Ban, G. Pichler, M. Aymar, O. Dulieu, and W. Ernst, J. Phys. B **39**, S1191 (2006).
[16] P. S. Julienne, Faraday Discuss. **142**, 361 (2009).
[17] D. Borsalino, B. Londono-Florez, R. Vexiau, O. Dulieu, N. Bouloufa-Maafa, and E. Luc-Koenig, Phys. Rev. A **90**, 033413 (2014).
[18] G. Krois, J. V. Pototschnig, F. Lackner, and W. E. Ernst, J. Phys. Chem. A **117**, 13719 (2013).
[19] G. Krois, F. Lackner, J. V. Pototschnig, T. Buchsteiner, and W. E. Ernst, Phys. Chem. Chem. Phys. **16**, 22373 (2014).

[20] J. V. Pototschnig, G. Krois, F. Lackner, and W. E. Ernst, J. Mol. Spectrosc. **310**, 126 (2015).
[21] J. Gerschmann, E. Schwanke, A. Pashov, H. Knöckel, S. Ospelkaus, and E. Tiemann, Phys. Rev. A **96**, 032505 (2017).
[22] E. Schwanke, H. Knöckel, A. Stein, A. Pashov, S. Ospelkaus, and E. Tiemann, J. Phys. B **50**, 235103 (2017).
[23] A. Ciamei, J. Szczepkowski, A. Bayerle, V. Barbe, L. Reichsollner, S. M. Tzanova, C.-C. Chen, B. Pasquiou, A. Grochola, P. Kowalczyk, W. Jastrzebski, and F. Schreck, Phys. Chem. Chem. Phys. **20**, 26221 (2018).
[24] P. S. Żuchowski, J. Aldegunde, and J. M. Hutson, Phys. Rev. Lett. **105**, 153201 (2010).
[25] V. Barbé, A. Ciamei, B. Pasquiou, L. Reichsollner, F. Schreck, P. S. Zuchowski, and J. M. Hutson, Nat. Phys. **14**, 881 (2018).
[26] D. Jaksch, V. Venturi, J. I. Cirac, C. J. Williams, and P. Zoller, Phys. Rev. Lett. **89**, 040402 (2002).
[27] S. Stellmer, B. Pasquiou, R. Grimm, and F. Schreck, Phys. Rev. Lett. **109**, 115302 (2012).
[28] A. Ciamei, A. Bayerle, C.-C. Chen, B. Pasquiou, and F. Schreck, Phys. Rev. A **96**, 013406 (2017).
[29] R. Guérout, M. Aymar, and O. Dulieu, Phys. Rev. A **82**, 042508 (2010).
[30] P. S. Żuchowski, R. Guérout, and O. Dulieu, Phys. Rev. A **90**, 012507 (2014).
[31] B. Pasquiou, A. Bayerle, S. M. Tzanova, S. Stellmer, J. Szczepkowski, M. Parigger, R. Grimm, and F. Schreck, Phys. Rev. A **88**, 023601 (2013).
[32] J. V. Pototschnig, G. Krois, F. Lackner, and W. E. Ernst, J. Chem. Phys. **141**, 234309 (2014).
[33] J. Jiang, Y. Chen, and J. Mitroy, J. Phys. B **46**, 125004 (2013).
[34] T. Chen, S. Zhu, X. Li, J. Qian, and Y. Wang, Phys. Rev. A **89**, 063402 (2014).
[35] V. Kokoouline, O. Dulieu, R. Kosloff, and F. Masnou-Seeuws, J. Chem. Phys. **110**, 9865 (1999).
[36] V. Kokoouline, O. Dulieu, R. Kosloff, and F. Masnou-Seeuws, Phys. Rev. A **62**, 032716 (2000).
[37] V. Kokoouline, O. Dulieu, and F. Masnou-Seeuws, Phys. Rev. A **62**, 022504 (2000).
[38] K. Willner, O. Dulieu, R. Kosloff, and F. Masnou-Seeuws, J. Chem. Phys. **120**, 548 (2004).
[39] L. K. Sorensen, S. Knecht, T. Fleig, and C. M. Marian, J. Phys. Chem. A **113**, 12607 (2009).
[40] M. Aymar, O. Dulieu, and F. Spiegelman, J. Phys. B **39**, S905 (2006).
[41] P. Pillet, A. Crubellier, A. Bleton, O. Dulieu, P. Nosbaum, I. Mourachko, and F. Masnou-Seeuws, J. Phys. B **30**, 2801 (1997).
[42] E. Luc-Koenig, M. Vatasescu, and F. Masnou-Seeuws, Eur. Phys. J. D **31**, 239 (2004).
[43] A. Fioretti, C. Amiot, C. M. Dion, O. Dulieu, M. Mazzoni, G. Smirne, and C. Gabbanini, Eur. Phys. J. D **15**, 189 (2001).
[44] K. Bergmann, N. V. Vitanov, and B. W. Shore, J. Chem. Phys. **142**, 170901 (2015).
[45] E. A. Shapiro, M. Shapiro, A. Pe'er, and J. Ye, Phys. Rev. A **75**, 013405 (2007).
[46] F. Deuretzbacher, K. Plassmeier, D. Pfannkuche, F. Werner, C. Ospelkaus, S. Ospelkaus, K. Sengstock, and K. Bongs, Phys. Rev. A **77**, 032726 (2008).
[47] A. Ciamei and F. Schreck (private communication).
[48] J. G. Danzl, M. J. Mark, E. Haller, M. Gustavsson, R. Hart, J. Aldegunde, J. M. Hutson, and H.-C. Nägerl, Nat. Phys. **6**, 265 (2010).